Effect of Twin Boundary Density on Mechanical Response and Dislocation Evolution in a Nickel-Based Superalloy: A Molecular Dynamics Study

Hamed Heydari [a], Mojtaba Zolfaghari [a *]

*** m-zolfaghari@araku.ac.ir**

[a] Department of Mechanical Engineering, Arak University, Arak, Iran

Abstract

Twin-boundary engineering provides an effective approach for tailoring the mechanical response of nickel-based superalloys; however, the density-dependent atomistic mechanisms remain insufficiently understood in explicit dual-phase γ/γ′ microstructures. Molecular dynamics simulations were performed on a single-crystal model and models containing one, two, and eight twin boundaries oriented perpendicular to the loading direction. The tensile response was analyzed in conjunction with dislocation-density evolution, microstructural changes, and Constructed-surface-mesh analysis to characterize crack initiation and growth. The TB1 model exhibited higher yield stress and strain than the single-crystal model because the isolated twin boundary impeded dislocation motion. In contrast, TB2 and TB8 yielded at lower stresses and strains because the increased twin-boundary density introduced additional preferential nucleation sites at the twin boundaries and twin-boundary/γ–γ′ interface intersections. Despite its earlier yielding, TB2 exhibited the highest ultimate stress among all models and the highest ultimate strain among the twinned models. This behavior was attributed to deformation partitioning between two comparatively stable twin boundaries, which promoted distributed precipitate shearing, dislocation storage, and sustained strain hardening. TB8 exhibited the highest initial dislocation density, followed by a decrease during plastic deformation associated with twin-boundary migration, defect rearrangement, and strain localization. Constructed-surface-mesh analysis further showed that crack initiation was delayed to a strain of approximately 0.07356 in TB2, compared with approximately 0.066 in TB1 and TB8. Crack propagation occurred predominantly along the twin boundaries and γ/γ′ phase interfaces. These findings reveal a non-monotonic, density-dependent transition from barrier-controlled strengthening in TB1 to deformation-partitioning-assisted hardening in TB2 and boundary-migration-assisted, localization-dominated softening in TB8.

Keywords: Nickel-based superalloy, Twin boundary, Dislocation evolution, Dislocation density, Molecular dynamics

[DOI: 10.22068/ijmse.4525]

1. Introduction

Nickel-based superalloys are widely used in aerospace propulsion systems and industrial gas turbines, particularly in combustion chambers and high-pressure turbine components, because of their excellent mechanical strength at elevated temperatures. Their microstructure typically consists of a dual-phase γ/γ′ structure, comprising an FCC γ-Ni matrix and ordered $L1_2$ γ′-Ni_3Al precipitates [۱]. During service, these alloys are subjected to complex thermal and mechanical loading conditions; consequently, their long-term performance depends strongly on their mechanical properties and microstructural stability. Their service life is therefore closely governed by microstructural features and the associated deformation mechanisms [۲].

At the nanoscale, decreasing the grain size or characteristic sample dimensions generally increases the fraction of atoms located at interfaces and grain boundaries, thereby producing mechanical behavior that differs from that of bulk materials. Understanding the influence of grain boundaries is therefore essential for controlling the properties of metallic nanomaterials [۳]. Twin boundaries are a special class of grain boundaries characterized by high crystallographic symmetry and relatively low interfacial energy. They can impede dislocation motion and promote dislocation storage, thereby contributing to improved strength, ductility, and toughness [4-6]. Similar to conventional grain boundaries, twin boundaries may act as barriers to dislocation transmission and enhance material strength [۷]. They may also provide preferential planes for dislocation accumulation, transmission, or slip, which can contribute to plastic deformation and ductility [۸]. Molecular dynamics simulations are particularly suitable for examining these atomic-scale processes because they enable direct analysis of dislocation activity, interface interactions, and deformation mechanisms under controlled loading conditions [۲].

Zhang and Jiang used molecular dynamics simulations to investigate plastic deformation in nanotwinned polycrystalline copper under tensile loading. Samples with twin boundaries oriented parallel or perpendicular to the loading direction exhibited strain hardening because dislocation–twin-boundary interactions restricted dislocation motion. By contrast, samples containing inclined twin boundaries showed softening behavior owing to the limited interaction between dislocations and twin boundaries and the activation of slip on planes parallel to the twin-boundary plane [۹]. Song and Li examined the combined effects of twin-boundary spacing and temperature on the deformation behavior of nanotwinned magnesium. They reported a marked change in mechanical response when the twin spacing decreased below 2.9 nm, while the yield strength decreased with increasing temperature. At relatively high temperatures, softening was also observed when the twin-boundary spacing exceeded 7.8 nm. Their results linked the yield strength to the repulsive interaction between dislocations and twin boundaries [۱۰].

Stukowski et al. investigated the influence of twin boundaries on the tensile deformation of copper and palladium nanocrystals using atomistic simulations. Twin boundaries produced a strengthening effect in copper but a softening effect in palladium, demonstrating that the mechanical response to nanotwinning is material dependent [11]. Gao et al. studied Ni–Co alloy nanopillars containing twin boundaries perpendicular to the loading direction. When more than two twin boundaries were introduced, dislocation–twin-boundary interactions became increasingly significant, while twin-boundary migration and interaction increased the dislocation density. They also found that increasing the strain rate shifted the dominant deformation mechanism from dislocation–twin-boundary interaction to twin-boundary migration [۳].

Zhang et al. investigated the effect of perpendicular twin-boundary spacing on the tensile deformation of single-crystal $Al_{0.1}CoCrFeNi$ using molecular dynamics simulations. As the twin spacing decreased, the dominant deformation mechanism gradually changed from dislocation slip accompanied by stacking faults and secondary twinning to deformation governed by amorphous-phase transformation [۱۲]. Tran further examined the

[DOI: 10.22068/ijmse.4525]

effects of grain size and twin-boundary spacing on the tensile properties of polycrystalline $Cu_{50}Ni_{50}$ and showed that twin boundaries significantly suppressed the formation and propagation of stacking faults [۱۳].

Wang et al. investigated the influence of twin boundaries perpendicular to the loading direction on the plastic deformation and fracture behavior of nanotwinned Ni_3Al using molecular dynamics simulations and an atomistic crack model. They found that decreasing the twin-boundary spacing simultaneously enhanced the strength, ductility, and fracture toughness. The twin boundaries impeded dislocation propagation, while dislocation activity contributed to crack-tip blunting [۱۴]. Experimental observations have also indicated a close correspondence between twin boundaries and precipitate formation in nickel-based superalloys [8]. Zhang et al. identified a twinning-related degradation mechanism under service-relevant conditions. By combining multiscale microstructural and mechanical characterization with density functional theory calculations, they showed that twinning promoted early dislocation activity and strain localization during mechanical loading [۱۵]. Shi et al. experimentally examined the microstructural, mechanical, and fracture behavior of nickel-based superalloys containing twin boundaries, together with density functional theory calculations. Their results indicated that twin boundaries promoted early dislocation activity and localized deformation and could therefore act as preferential sites for crack initiation [16].

Despite these advances, previous studies on twin boundaries in nickel-based superalloys have been predominantly experimental. Although such investigations provide valuable information on the microstructure and mechanical response, they cannot continuously resolve the atomic-scale evolution of dislocations, interfaces, and local damage during deformation. A detailed atomistic understanding of how the number and spacing of twin boundaries affect plastic deformation and fracture in dual-phase γ/γ′ microstructures therefore remains necessary. In the present study, molecular dynamics simulations were used to investigate the tensile behavior of a single-crystal nickel-based superalloy and models containing one, two, and eight twin boundaries oriented perpendicular to the loading direction. The stress–strain response of the single-crystal and TB1 models was first compared. The mechanisms of dislocation nucleation, motion, interaction, and slip, together with crack initiation and propagation, were then analyzed and compared among the TB1, TB2, and TB8 models.

To the best of the authors' knowledge, twin-boundary-density-dependent deformation and fracture mechanisms have not previously been systematically quantified at the atomic scale in an explicit dual-phase γ/γ′ nickel-based superalloy. The novelty of this study lies in quantitatively linking the number and spacing of twin boundaries to dislocation nucleation, evolution, and storage; twin-boundary migration; deformation partitioning; and crack initiation and growth. This framework reveals a density-dependent transition from barrier-controlled strengthening in TB1 to deformation-partitioning-assisted hardening in TB2 and, finally, to boundary-migration-assisted and localization-dominated softening in TB8 within the same γ-Ni/γ′-Ni_3Al microstructural model.

2. Simulation Details

The nickel-based superalloy model consisted of a γ matrix composed of Ni atoms and a γ′ precipitate phase composed of the intermetallic compound Ni_3Al, with lattice parameters a_γ and $a_{\gamma'}$, respectively. The γ′ volume fraction was 72.9%, consistent with the reported microstructure of nickel-based superalloys [۱۷]. A three-dimensional Ni/Ni_3Al model containing a twin boundary was constructed using Atomsk software [۱۸]. Because the γ matrix and γ′ precipitates had different equilibrium lattice parameters, a coherency mismatch developed at the γ/γ′ phase interfaces. This mismatch generated interfacial stress fields and led to the formation of an initial misfit-dislocation network during structural relaxation. The lattice mismatch, δ, was calculated using Eq. (1) [۱۹]:

$$\delta = 2 * \frac{a_{\gamma'} - a_\gamma}{a_{\gamma'} + a_\gamma} \quad (1)$$

[DOI: 10.22068/ijmse.4525]

where a_γ and $a_{\gamma'}$ denote the lattice parameters of the γ-Ni matrix and γ′-Ni_3Al precipitate, respectively. Substituting $a_\gamma = 3.52$Å and $a_{\gamma'} = 3.572$ into Eq. (1) yielded a lattice mismatch of approximately 1.5%. This mismatch produced the initial γ/γ′ interfacial misfit-dislocation network during structural relaxation. Therefore, the dislocations detected before tensile loading were primarily associated with the relaxed phase-misfit network rather than with loading-induced plastic deformation. During subsequent tensile loading, the stressed γ/γ′ interfaces associated with this network also served as preferential sites for the nucleation of additional dislocations. The crystallographic orientations of the x, y, and z axes were [11-2], [−110], and [111], respectively. The twin region was generated by applying a continuous atomic displacement field symmetric about the (111) plane, while the surrounding grain remained unchanged. Accordingly, the z-axis was normal to the twin-boundary plane. As shown in Fig. 1, the Ni and Al atoms are represented in blue and red, respectively. The investigated models contained one, two, or eight twin boundaries oriented perpendicular to the loading direction. Each model had dimensions of 243.873 × 199.121 × 344.888 Å³. The model without a twin boundary contained 1,492,564 atoms, whereas the models containing twin boundaries perpendicular to the loading direction contained 1,491,540 atoms. Tensile simulations were performed using LAMMPS [۲۰]. Interatomic interactions in the Ni–Al system were described using an embedded-atom method (EAM) potential [۲۱], which has been widely employed to investigate the deformation mechanisms of nickel-based superalloy nanostructures [22-24]. Periodic boundary conditions were applied along the x- and y-directions, whereas the z-direction was non-periodic. Atomic layers with a thickness of 10 Å were defined at the top and bottom of each model to impose the boundary constraints and tensile loading.

Before loading, the models were equilibrated at 300 K for 120 ps in the NVT ensemble using a Nosé–Hoover thermostat [۲۵]. Tensile deformation was subsequently applied by moving the upper atomic layer along the z-direction at a velocity corresponding to a constant strain rate of 1×10^9 s^{-1}. The temperature was maintained at 300 K using the Nosé–Hoover thermostat throughout the tensile simulations. A time step of 2 fs was used in all simulations.

The atomic configurations were visualized and analyzed using OVITO [۲۶]. The dislocation extraction algorithm (DXA) [۲۷] was employed to identify dislocation types and quantify their density and evolution during deformation. Common neighbor analysis was used to characterize changes in the local crystal structure. Atoms identified as FCC, BCC, and HCP were displayed in green, blue, and red, respectively. Finally, constructed surface-mesh analysis was used to detect and visualize cracks and internal discontinuities, with the corresponding surface regions displayed in turquoise.

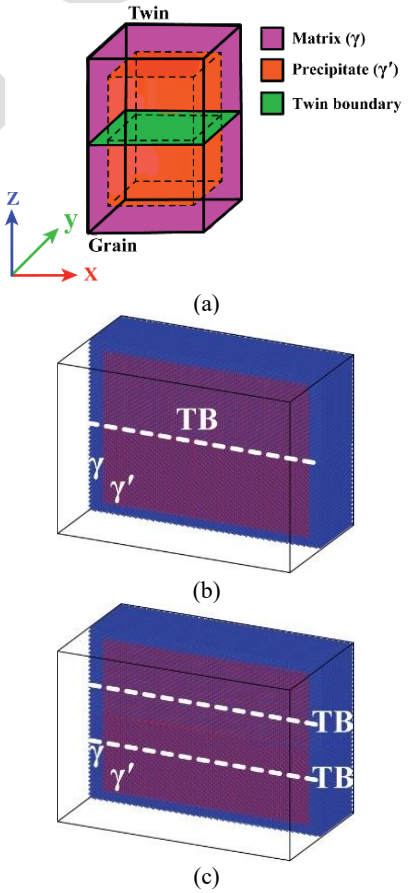

[DOI: 10.22068/ijmse.4525]

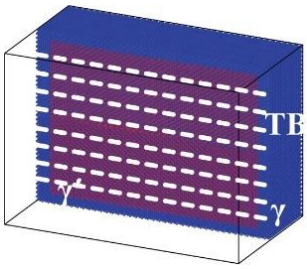

(d)

Fig. 1. (a) Three-dimensional atomic model containing a single twin boundary perpendicular to the loading direction; cross-sectional atomic configurations of the models containing (b) one, (c) two, and (d) eight twin boundaries perpendicular to the loading direction.

3. Results and Discussion

3.1. Single Twin Boundary Perpendicular to the Loading Direction

3.1.1. Stress–Strain Response

To investigate the influence of a single twin boundary on the mechanical behavior of the nickel-based superalloy, tensile simulations were performed on the single-crystal (SC) and single-twin-boundary (TB1) models. Figure 2 presents the stress–strain responses of both models, together with the dislocation density–strain, dislocation length–strain, and local-structure atom population–strain curves and the corresponding atomic configurations of the TB1 model. The differences between the two stress–strain curves demonstrate that the twin boundary affects the tensile response of the superalloy.

Up to a strain of approximately 0.045, the stress in both models increased almost linearly with strain, indicating elastic deformation. The elastic modulus of the TB1 model, calculated from the slope of the linear elastic region, was approximately 1.8% lower than that of the SC model. This slight reduction indicates that the presence of the twin boundary decreased the elastic stiffness of the model. Beyond the linear region, the two stress–strain curves exhibited different nonlinear responses, and the stress continued to increase until the peak value was reached, indicating the occurrence of strain hardening after the onset of plastic deformation.

The onset of dislocation nucleation was adopted as the criterion for determining the yield stress and yield strain. As shown in Fig. 2(a), the yield stresses of the SC and TB1 models were 12.97 and 13.65 GPa, respectively, with corresponding yield strains of 0.0479 and 0.0501. Therefore, the twin boundary perpendicular to the loading direction increased both the yield stress and yield strain relative to the single-crystal model [9, 28]. This result indicates that an isolated twin boundary can act as a strengthening feature under uniaxial tensile loading by increasing the resistance to the onset of plastic deformation [٢٩].

After yielding, continued dislocation nucleation, motion, and multiplication enabled further plastic deformation. The stress increased with strain during this stage, confirming the occurrence of strain hardening. Subsequently, the stress reached the ultimate tensile strength, at which the primary crack initiated. The ultimate stresses of the SC and TB1 models were 15.728 and 15.540 GPa, respectively, at corresponding strains of 0.08061 and 0.06536. Thus, although the twin boundary enhanced the yield response, both the ultimate stress and ultimate strain of the TB1 model were lower than those of the SC model. The decrease in stress after the peak value indicates crack propagation and eventual fracture.

The tensile toughness was calculated by integrating the area under each stress–strain curve [٣٠]. The toughness values of the SC and TB1 models were 0.134 and 0.060 GPa, respectively. Accordingly, under the present simulation conditions, the twin boundary perpendicular to the loading direction reduced the energy-absorption capacity and toughness of the superalloy [٢٨].

3.1.2. Deformation Mechanisms of the TB1 Model

Up to a strain of approximately 0.05, the stress in the TB1 model increased nearly linearly, while the length and density of the initial dislocations associated with the γ/γ′ phase-interface network and the twin boundary remained almost constant (Figs. 2(a) and 2(b)). The populations of atoms with different local crystal structures also showed no noticeable variation, and the model retained its initial atomic configuration (Fig. 2(c)). These

[DOI: 10.22068/ijmse.4525]

observations confirm that the model remained within the elastic-deformation regime, as illustrated in Fig. 2(d). Yielding occurred at a strain of 0.05011, where a slight change in the slope of the stress–strain curve was accompanied by an increase in the density of partial dislocations (Figs. 2(a) and 2(b)). At the onset of yielding, dislocations nucleated at the γ/γ′ phase interfaces in both the grain and twin regions and propagated obliquely through the matrix toward the twin boundary [۳۱]. With continued slip, some of these dislocations interacted with the twin boundary, demonstrating that it acted as an obstacle to dislocation motion (Fig. 2(e)).

As the strain and plastic deformation increased, the number of HCP atoms increased, whereas the number of FCC atoms decreased (Fig. 2(c)). Additional dislocations nucleated at the intersections between the twin boundary and the γ/γ′ phase interfaces. These dislocations initially sheared the γ′ precipitates in the grain region and subsequently propagated into the twin region, thereby sustaining plastic deformation. Moreover, some dislocations nucleated at the phase interfaces crossed the precipitates and subsequently interacted with the twin boundary, inducing local twin-boundary migration (Fig. 2(f)).

Most of the gliding dislocations within the matrix and precipitate regions exhibited mixed character. With continued deformation, their motion was increasingly restricted by the γ/γ′ phase interfaces, particularly near the upper and lower regions of the precipitates (Figs. 2(g) and 2(h)). The twin boundary also impeded the transmission of several dislocations across the boundary (Figs. 2(g) and 2(h)). Therefore, between the yield and ultimate strains, both the twin boundary and the phase interfaces contributed to the strengthening response. However, the observed dislocation trajectories indicate that the twin boundary provided a stronger barrier than the phase interfaces and prevented the transmission of most dislocations that reached it.

The active slip planes in the matrix of the grain region were $(\bar{1}1\bar{1})$, (111), and $(1\bar{1}\bar{1})$, whereas those in the precipitates of the grain region were $(\bar{1}1\bar{1})$, (111), and $(\bar{1}\bar{1}1)$. In the twin region, slip occurred on $(\bar{1}\bar{1}1)^T$, $(\bar{1}1\bar{1})^T$, and $(1\bar{1}\bar{1})^T$. As shown in Fig. 2(a), the model remained in the strain-hardening regime up to a strain of approximately 0.061. During this stage, Shockley partial dislocations sheared an increasing number of γ′ precipitates and interacted with dislocations gliding on intersecting $\{111\}$ planes. These dislocation–dislocation interactions resulted in the formation of sessile stair-rod dislocations. A representative crystallographic reaction describing the formation of a stair-rod dislocation [32, 33] is presented in Eq. (2) and illustrated in Fig. 2(i):

$$\frac{1}{6}[1-1-2]_{(-11-1)} + \frac{1}{6}[-121]_{(-1-11)} \rightarrow \frac{1}{6}[01-1] \quad (2)$$

In Eq. (2), the two terms on the left-hand side represent Shockley partial dislocations gliding on two intersecting $\{111\}$ planes, while the subscripts denote their respective slip planes. Conservation of the Burgers vector yields the $1/6\langle 110\rangle$-type reaction product shown on the right-hand side. Because the resulting dislocation cannot readily glide on either of the original $\{111\}$ planes, it is classified as a sessile stair-rod dislocation. Its formation immobilized part of the mobile dislocation population and impeded subsequent slip. This crystallographic reaction therefore accounts for the increases in the density and total length of the stair-rod dislocations shown in Figs. 2(a) and 2(b), respectively. The accumulation of these sessile dislocations, together with the barrier effects of the twin boundary and the γ/γ′ phase interfaces, contributed directly to the strain-hardening response of the TB1 model.

The constructed surface-mesh area began to increase from zero at a strain of $\varepsilon = 0.06536$ (Fig. 2(b)), corresponding to the attainment of the peak stress in the stress–strain curve (Fig. 2(a)). At this stage, dislocation motion along the twin boundary generated a local stress concentration, resulting in the initiation of the primary crack at the twin boundary within the γ′ precipitate [۱۵] (Fig. 2(j)). With further loading, plastic deformation continued through the nucleation

[DOI: 10.22068/ijmse.4525]

and slip of dislocations from both the twin-boundary/phase-interface intersections and the γ/γ′ phase interfaces. The twin boundary impeded the motion of these dislocations, leading to further stress accumulation along the boundary. Consequently, additional cracks formed at other locations along the twin boundary within the precipitate region, as shown in Figs. 2(k) and 2(l).

Following the post-peak stress drop, crack propagation at a strain of 0.069 was accompanied by intense plastic deformation around the crack tip. This crack-tip plasticity increased the population of Shockley partial dislocations, resulting in a corresponding increase in the number of HCP atoms and a decrease in the number of FCC atoms (Figs. 2(a)–2(c)). The continued motion of the $1/6[1\bar{1}\bar{2}](\bar{1}1\bar{1})$, $1/6[\bar{2}11](111)$, $1/6[\bar{1}21](\bar{1}\bar{1}1)$, and $1/6[\bar{1}\bar{1}\bar{2}]^T(\bar{1}1\bar{1})^T$ dislocations promoted crack growth along the twin boundary through both the γ′ precipitate and γ matrix, as illustrated in Fig. 2(l). Final fracture subsequently occurred along the twin boundary (Fig. 2(m)).

During plastic deformation, slip planes and stacking faults were more pronounced in the precipitate within the twin region than in the corresponding grain region. During crack propagation, however, the extent of slip and stacking-fault formation increased substantially in both regions. The dominant slip planes activated in the matrix and precipitate throughout the deformation of the TB1 model are schematically illustrated in Fig. 2(n), in agreement with previous studies [34, 35].

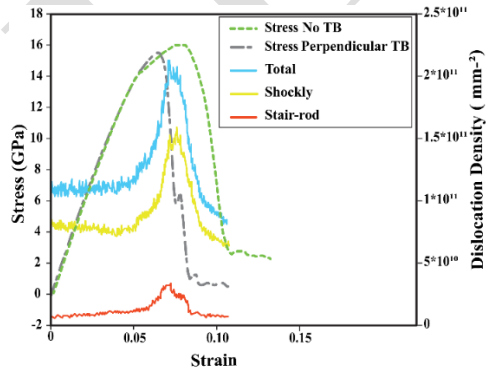

(a)

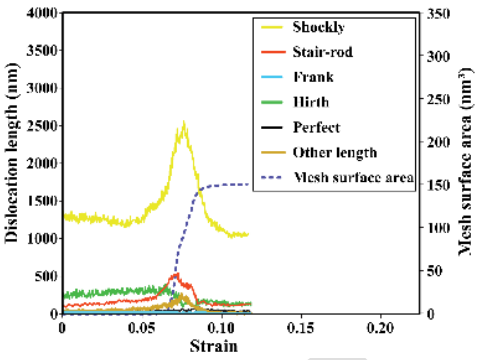

(b)

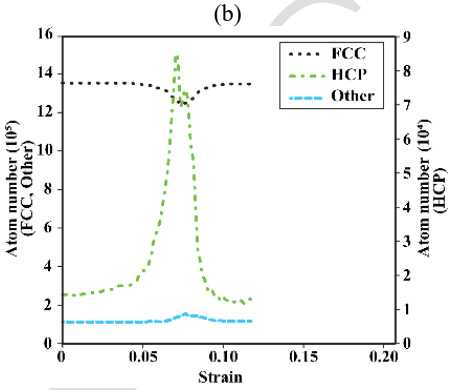

(c)

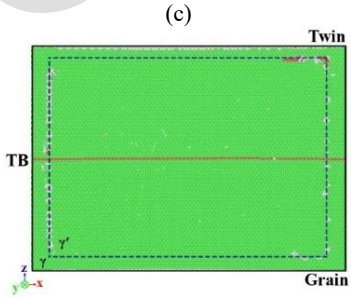

(d)

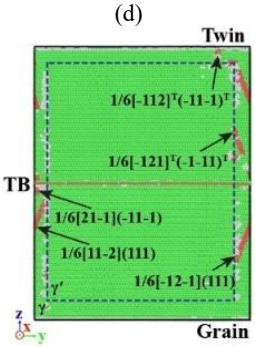

(e)

[DOI: 10.22068/ijmse.4525]

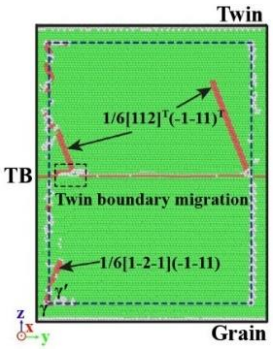

(f)

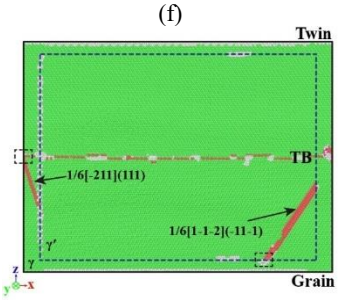

(g)

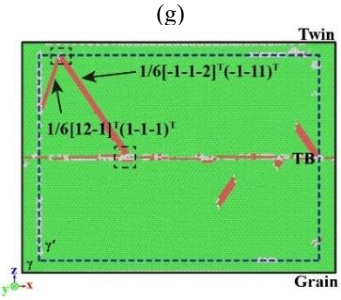

(h)

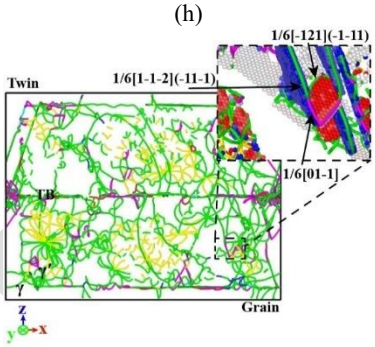

(i)

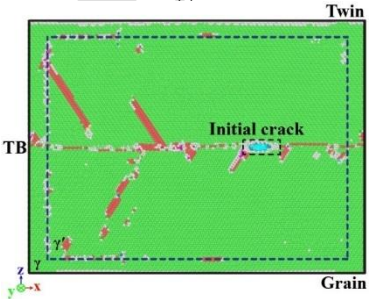

(j)

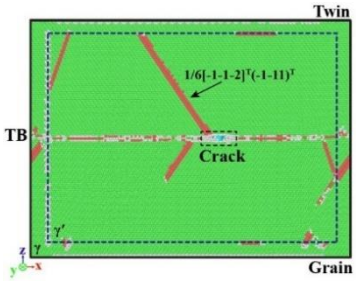

(k)

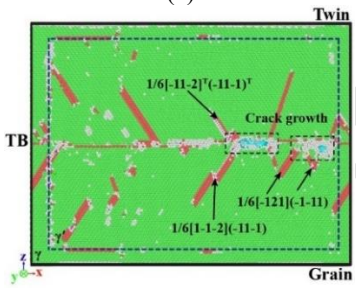

(l)

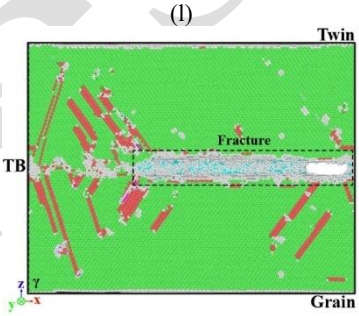

(m)

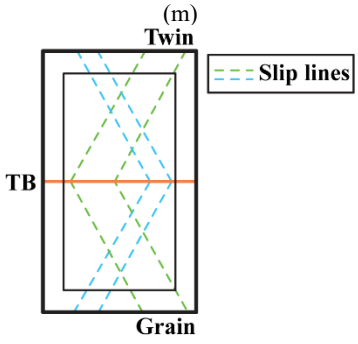

(n)

Fig. 2. Mechanical response and deformation evolution of the TB1 model: (a) dislocation density–strain and stress–strain curves for TB1, together with the stress–strain curve of the single-crystal model; (b) evolution of dislocation length with strain; (c) evolution of local-structure atom populations with strain; and (d–m) two-dimensional atomic configurations and cross-sectional views showing dislocation evolution, plastic deformation, crack initiation, and fracture at $\varepsilon =$ 0.02833(d), 0.05186 (e), 0.05446 (f), 0.05838 (g), 0.059 (h), 0.061 (i), 0.06536 (j), 0.0671 (k), 0.069 (l), and 0.0962 (m). FCC atoms were omitted in panels (d–i) to improve the visibility of the dislocation structures; in the enlarged view at $\varepsilon = 0.061$, the active slip planes are shown in blue, red, and white for visual distinction. (n)

[DOI: 10.22068/ijmse.4525]

Schematic representation of the dominant slip planes in the TB1 model.

3.2. Effect of Twin-Boundary Density

3.2.1. Stress–Strain Responses of the TB1, TB2, and TB8 Models

Figure 3(a) compares the stress–strain responses of the TB1, TB2, and TB8 models, in which the numeral following "TB" denotes the number of twin boundaries oriented perpendicular to the loading direction. Up to a strain of approximately 0.024, the stress in all three models increased nearly linearly with increasing strain. The slopes of the elastic regions were essentially identical, indicating that increasing the number of perpendicular twin boundaries had no significant effect on the Young's modulus.

Beyond a strain of 0.02443, the TB8 stress–strain curve deviated from linearity and continued to increase toward the peak stress, indicating the onset of plastic deformation followed by strain hardening. The onset of dislocation nucleation was adopted as the criterion for determining the yield stress and yield strain. As shown in Fig. 3(a), the yield stresses of the TB1, TB2, and TB8 models were 13.65, 10.852, and 6.407 GPa, respectively, with corresponding yield strains of 0.0501, 0.04283, and 0.02443. In contrast to TB1, both TB2 [۳] and TB8 exhibited lower yield stresses and strains than the single-crystal model.

The progressive reduction in yield stress and strain with increasing twin-boundary density can be attributed to a transition in the dominant role of the twin boundaries from barriers to dislocation motion to preferential sites for dislocation nucleation. In TB1, the isolated twin boundary primarily impeded the transmission of dislocations nucleated at the γ/γ′ phase interfaces. Consequently, a relatively high applied stress was required to initiate extensive plastic deformation. By contrast, increasing the number of twin boundaries introduced additional twin-boundary planes and twin-boundary/γ–γ′ interface intersections, where local stress concentrations developed. These regions, particularly the twin-boundary segments located within the γ′ precipitates, acted as preferential sites for the early nucleation of partial dislocations. As a result, dislocation activity began at lower applied strains in TB2 and TB8.

This source-dominated behavior was most pronounced in TB8 because the reduced twin spacing generated interacting local stress fields and a larger number of closely spaced dislocation-nucleation sites. Consequently, the enhanced nucleation activity outweighed the barrier effect of the twin boundaries, accounting for the progressive decrease in yield stress and strain from TB1 to TB2 and TB8 [3, 36], as illustrated in Figs. 3(a)–3(c).

After yielding, continued dislocation motion and multiplication produced further plastic deformation and strain hardening in all three models. The stress subsequently reached the ultimate tensile strength, coinciding with the onset of primary crack formation. The ultimate stresses of the TB1, TB2, and TB8 models were 15.540, 16.27, and 14.64 GPa, respectively, at corresponding strains of 0.06536, 0.07356, and 0.06642. TB2 therefore exhibited the highest ultimate stress among all investigated models and the highest ultimate strain among the twinned models. Among the twinned models, the ultimate stress followed the order TB2 > TB1 > TB8, whereas the ultimate strain followed the order TB2 > TB8 > TB1. In all cases, the post-peak decrease in stress indicates crack propagation and eventual fracture.

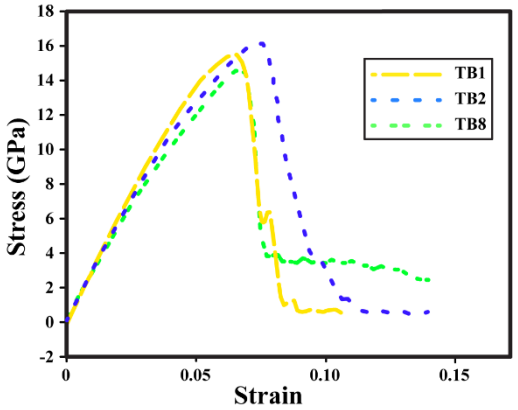

(a)

[DOI: 10.22068/ijmse.4525]

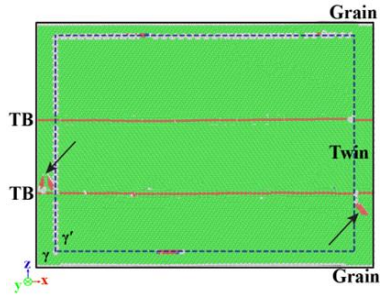

(b)

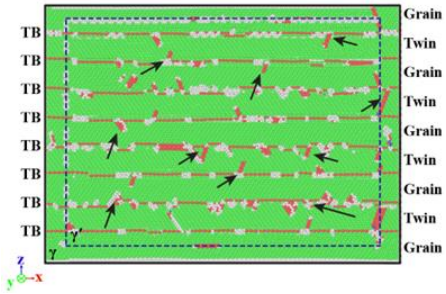

(c)

Fig. 3. (a) Stress–strain responses of the TB1, TB2, and TB8 models; two-dimensional atomic configurations and corresponding cross-sectional views showing dislocation evolution and deformation in (b) TB2 at $\varepsilon = 0.0429$and (c) TB8 at $\varepsilon = 0.032$.

3.2.۲. Effect of Twin-Boundary Density on Dislocation-Density Evolution

Figure 4 compares the evolution of dislocation density with strain in the TB1, TB2, and TB8 models. The initial dislocation density increased markedly with twin-boundary density, following the order TB8 > TB2 > TB1. This trend can be attributed to the greater number of twin-boundary planes, intersections between the twin boundaries and γ/γ′ phase interfaces, and local perturbations of the γ/γ′ misfit-dislocation network. Consequently, models with higher twin-boundary densities contained larger initial populations of line defects and potential dislocation-nucleation sites before the onset of extensive plastic deformation. In TB1, the dislocation density remained nearly constant up to the yield strain of approximately 0.0501, indicating that the initial dislocations were predominantly associated with the relaxed γ/γ′ interfacial network and that sustained nucleation of additional dislocations had not yet begun. TB2 exhibited a moderate increase in dislocation density before yielding, suggesting localized precursor activity at the twin boundaries and their intersections with the phase interfaces. This pre-yield activity was considerably more pronounced in TB8, where the reduced twin spacing promoted interactions between local stress fields and activated dislocation sources at substantially lower applied strains. This behavior is consistent with the lowest yield stress and strain observed in TB8.

After yielding, the initial evolution of dislocation density in TB1 and TB2 was governed primarily by dislocation multiplication and storage. In TB1, the dislocation density increased sharply after yielding because dislocations nucleated at the γ/γ′ phase interfaces and twin-boundary/phase-interface intersections, propagated through the γ matrix and γ′ precipitates, and were subsequently impeded by the twin boundary, phase interfaces, and other dislocations. These interactions increased the stored dislocation content, promoted the formation of sessile stair-rod dislocations, and contributed to the strain-hardening response. However, crack initiation in TB1 occurred at a strain of approximately 0.06536, before the dislocation density reached its maximum value. Therefore, the upper portion of the density peak cannot be attributed solely to relatively homogeneous plastic deformation; it also includes a substantial contribution from crack-tip plasticity and the emission of additional dislocations from the highly stressed region surrounding the growing crack. After the peak, the dislocation density decreased rapidly because crack propagation caused stress relaxation, dislocation annihilation, absorption of dislocations at newly formed free surfaces, and a reduction in the effective load-bearing volume.

TB2 exhibited a broader and more sustained increase in dislocation density than TB1. This response indicates that the two twin boundaries provided not only additional nucleation sites but also a wider strain interval over which the generated dislocations could be stored and redistributed. The twin boundaries partitioned the model into distinct deformation regions, restricted direct slip transmission, and redirected dislocations along the boundaries and toward successive γ′ precipitates. Simultaneously, some dislocations were annihilated after interacting with the upper twin boundary or the γ/γ′ phase

[DOI: 10.22068/ijmse.4525]

interfaces. The resulting dislocation-density curve therefore reflects competition among dislocation nucleation, storage, redistribution, and annihilation rather than a simple monotonic multiplication process. Because crack initiation in TB2 occurred near its ultimate strain of 0.07356, the final portion of the broad maximum also included dislocation activity associated with crack-tip plasticity. Compared with TB1, the slower post-peak decrease indicates that distributed plastic deformation remained active around the crack tip, twin boundaries, and γ/γ′ phase interfaces over a broader strain range. This behavior is consistent with the highest ultimate stress among all investigated models and the highest ultimate strain among the twinned models.

The dislocation-density evolution in TB8 differed fundamentally from that observed in TB1 and TB2. Following the early onset of plastic deformation, the dislocation density initially increased but subsequently decreased with further strain, although the model remained within the plastic-deformation regime. This behavior indicates that plastic deformation in TB8 was not governed solely by continuous dislocation storage. The narrow spacing between adjacent twin boundaries substantially reduced the mean free path of gliding dislocations and increased the frequency of dislocation–twin-boundary interactions. Repeated dislocation impingement promoted local twin-boundary migration, allowing part of the imposed strain to be accommodated through boundary displacement. Twin-boundary migration may also have absorbed, rearranged, or eliminated dislocation segments and stacking-fault structures, thereby reducing the line-defect density detected by the dislocation extraction algorithm despite the continued accumulation of plastic strain. A small secondary fluctuation at larger strains may be associated with renewed dislocation nucleation at the phase interfaces or within the crack-tip region. Nevertheless, the overall decreasing trend indicates a transition from dislocation-storage-dominated plasticity to boundary-migration-assisted deformation and damage localization in TB8.

Overall, increasing the twin-boundary density did not continuously enhance the ability of the microstructure to retain dislocations throughout deformation. A higher twin-boundary density increased the initial line-defect content and promoted earlier activation of dislocation sources, thereby reducing the yield stress and strain. At the intermediate density represented by TB2, the twin boundaries provided an effective balance among dislocation nucleation, blocking, storage, redistribution, and annihilation, resulting in sustained strain hardening. At the highest density represented by TB8, enhanced twin-boundary migration and localized deformation limited stable dislocation storage and promoted earlier damage development. The dislocation-density curves therefore reveal a density-dependent transition from barrier- and storage-controlled plasticity to boundary-migration-assisted and localization-dominated deformation in the dual-phase γ/γ′ superalloy.

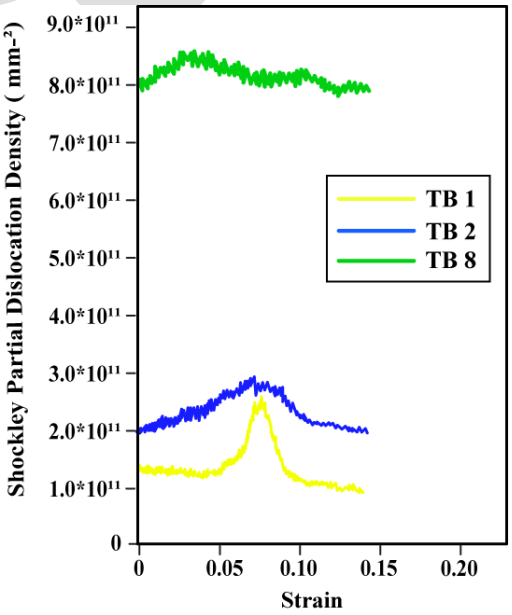

Fig. 4. Evolution of dislocation density with strain in the TB1, TB2, and TB8 models.

3.2.۳. Effect of Twin-Boundary Density on Damage Initiation and Crack Evolution

The evolution of the constructed surface-mesh area with strain provides a quantitative measure of damage initiation and subsequent crack growth in models containing different numbers of twin boundaries. As shown in Fig. 5, the surface-mesh

[DOI: 10.22068/ijmse.4525]

area remained approximately zero throughout the elastic and early plastic deformation stages, indicating that no detectable internal discontinuity or crack surface had formed. The first increase in this parameter occurred near the ultimate strain of each model. In TB1 and TB8, the surface-mesh area began to increase at strains of approximately 0.066, consistent with their ultimate strains of 0.06536 and 0.06642, respectively. By contrast, the onset of surface-mesh formation in TB2 occurred at a higher strain, close to its ultimate strain of 0.07356. This delayed damage initiation indicates that, although TB2 yielded earlier than TB1, the generated dislocations were stored and redistributed over a wider strain interval before a detectable crack formed. The two comparatively stable twin boundaries partitioned the model into separate deformation regions and restricted direct slip transmission, thereby promoting distributed precipitate shearing and delaying the localization of plastic deformation into a dominant crack.

After crack initiation, the constructed surface-mesh area increased rapidly in all three models; however, the subsequent growth behavior depended strongly on twin-boundary density. TB8 exhibited an early and steep increase in surface-mesh area, consistent with rapid damage localization near the closely spaced twin boundaries and twin-boundary/γ–γ′ interface intersections. The reduced twin spacing shortened the dislocation mean free path and promoted frequent dislocation interactions, local stress concentration, and the early coalescence of atomic-scale discontinuities. In TB1, damage also developed shortly after the ultimate strain because dislocation accumulation and motion along the isolated twin boundary promoted crack initiation within the γ′ precipitate region.

TB2 ultimately exhibited the largest surface-mesh area, reaching approximately 205 nm^2, compared with approximately 168 nm^2 and 160 nm^2 for TB1 and TB8, respectively. This larger final value should not be interpreted as evidence of lower resistance to crack initiation. Instead, it indicates that TB2 delayed the onset of cracking but subsequently underwent a more extensive damage-evolution process. The greater plastic-deformation capacity of TB2 allowed crack surfaces to develop along the upper and lower twin boundaries and the γ/γ′ phase interfaces before final separation. In contrast, failure in TB8 remained more strongly localized along the closely spaced twin boundaries.

The combined stress–strain and surface-mesh results demonstrate that the mechanisms governing yielding differed from those controlling damage initiation and crack propagation. TB8 yielded at a relatively low strain and rapidly developed localized damage because its high twin-boundary density introduced numerous dislocation-nucleation and stress-concentration sites. TB2 also yielded earlier than TB1; however, its deformation-partitioning capability delayed crack initiation and sustained strain hardening up to the highest ultimate stress among the investigated models. Thus, the intermediate twin-boundary density represented by TB2 provided the most effective balance among dislocation storage, distributed plasticity, and delayed damage localization. By contrast, the high twin-boundary density in TB8 promoted premature fracture through localization-dominated deformation. This non-monotonic relationship between twin-boundary density and damage evolution differs from the conventional interpretation of twin boundaries solely as strengthening barriers.

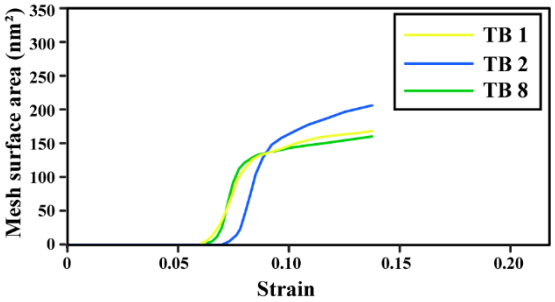

Fig. 5. Evolution of the constructed surface-mesh area with strain in the TB1, TB2, and TB8 models.

3.2.٤. Deformation Mechanisms of the TB2 and TB8 Models

Figures 6(a–g) illustrate the deformation evolution of the TB2 model. Up to a strain of approximately 0.042, the model retained its initial atomic configuration and remained within the elastic-deformation regime (Fig. 6(a)). Yielding occurred at a strain of 0.04283, after which

[DOI: 10.22068/ijmse.4525]

dislocations nucleated at the γ/γ′ phase interfaces, the twin boundaries, and their intersections in both the grain and twin regions. These dislocations propagated obliquely through the γ matrix toward the twin boundaries (Fig. 6(b)).

With increasing strain, dislocations nucleated predominantly at the lower twin boundary and at the twin-boundary/γ–γ′ interface intersections. They subsequently sheared the γ′ precipitates, first in the grain region and then in the twin region, thereby sustaining plastic deformation (Fig. 6(c)). Some dislocations also propagated through the matrix and precipitates, interacted with the upper twin boundary or the γ/γ′ phase interfaces, and were subsequently annihilated.

As loading continued, local stress concentrations developed at the twin boundaries, particularly at the lower boundary, because of the crystallographic misorientation between the grain and twin regions. Consequently, additional dislocations nucleated along the twin-boundary plane and propagated through both the γ matrix and γ′ precipitates in the grain and twin regions (Fig. 6(d)). With continued slip, their motion was increasingly impeded by the γ/γ′ phase interfaces, particularly near the upper and lower regions of the precipitates, as well as by the upper twin boundary (Fig. 6(d)). Therefore, between the yield and ultimate strains, both the twin boundaries and the phase interfaces contributed to the strengthening response of TB2.

Further loading activated additional dislocation sources at the lower twin boundary and the γ/γ′ phase interfaces. Moreover, dislocations that had been impeded during the earlier stages were redirected to glide along the twin boundaries. These processes promoted dislocation storage and distributed plastic deformation, enabling TB2 to attain the highest ultimate stress among all investigated models and the highest ultimate strain among the twinned models.

The post-yield response was governed not only by the onset of dislocation nucleation but also by the ability of the microstructure to store, redistribute, and constrain the generated dislocations. In TB1, some dislocations nucleated at the γ/γ′ phase interfaces, sheared the γ′ precipitates, and subsequently interacted with the twin boundary, resulting in local twin-boundary migration (Fig. 2(f)). This migration partially accommodated the imposed deformation and reduced the sustained barrier efficiency of the twin boundary. The subsequent strain hardening of TB1 therefore resulted from the combined resistance of the γ/γ′ phase interfaces, the remaining barrier effect of the twin boundary, and the formation of sessile stair-rod dislocations through dislocation–dislocation and dislocation–interface interactions (Fig. 2(i)).

In TB2, the atomic configurations indicated that the twin boundaries remained comparatively stable during the strain-hardening stage. These boundaries restricted direct slip transmission and partitioned the model into distinct deformation regions. Dislocations generated within each region were redirected along the twin boundaries and toward successive γ′ precipitates, thereby promoting distributed precipitate shearing, dislocation storage, and sustained strain hardening rather than immediate strain localization (Fig. 6(e)). This deformation-partitioning mechanism explains why TB2 exhibited the highest ultimate stress among all investigated models and the highest ultimate strain among the twinned models, despite yielding earlier than TB1 and the single-crystal model.

Most of the slipping dislocations in the γ matrix and γ′ precipitates exhibited mixed character. As shown in Fig. 3(a), TB2 reached its peak stress at a strain of $\varepsilon = 0.07356$. The atomic configuration shortly after the peak, at $\varepsilon = 0.07558$, shows that dislocations accumulated along the upper twin boundary and generated a local stress concentration, leading to primary crack initiation within the γ′ precipitate region [١٥] (Fig. 6(f)). With further loading, additional cracks formed at the γ/γ′ phase interfaces and the lower twin boundary. Nevertheless, crack propagation and final fracture occurred predominantly along the upper twin boundary (Fig. 6(g)).

A further increase in twin-boundary density transformed the beneficial deformation-partitioning behavior observed in TB2 into localization-dominated deformation in TB8. The narrow spacing between adjacent twin

[DOI: 10.22068/ijmse.4525]

boundaries substantially shortened the mean free path of gliding dislocations. Consequently, dislocations nucleated at the twin boundaries and twin-boundary/γ–γ′ interface intersections encountered neighboring boundaries after travelling only short distances. This behavior promoted rapid dislocation accumulation and intense local stress concentrations, particularly within the γ′ precipitates (Fig. 6(i)). The atomic configurations further suggest that repeated dislocation impingement induced more pronounced local twin-boundary displacement or migration in TB8 than in TB2 (Fig. 6(j)).

Rather than maintaining stable and sufficiently wide deformation regions, the closely spaced twin boundaries became preferential paths for localized plasticity and damage development. Thus, although individual twin boundaries continued to impede dislocation motion, their high density promoted early dislocation nucleation, boundary-mediated strain accommodation, and stress localization. These competing mechanisms limited sustained strain hardening and accelerated crack initiation along the twin boundaries and γ/γ′ phase interfaces, resulting in the lower ultimate stress and strain of TB8 (Figs. 6(k) and 6(l)).

Crack propagation in TB8 also followed the twin boundaries and γ/γ′ phase interfaces, although final fracture occurred predominantly along a twin boundary (Fig. 6(l)). The active slip planes in the matrix and precipitate phases of both the grain and twin regions in TB2 and TB8 were identical to those previously identified in TB1.

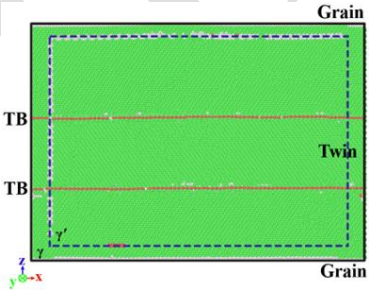

(a)

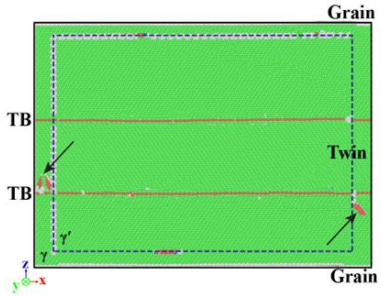

(b)

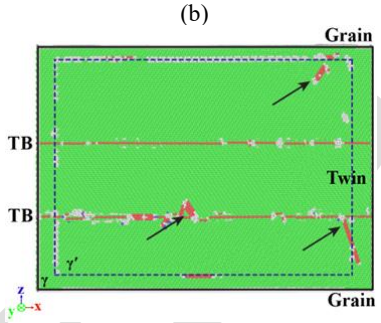

(c)

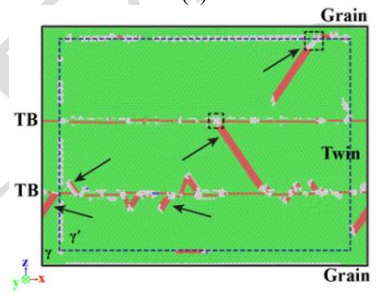

(d)

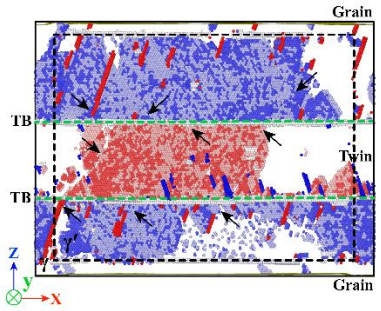

(e)

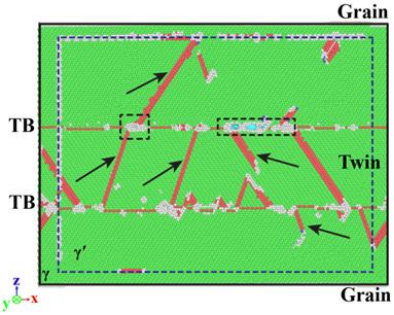

(f)

[DOI: 10.22068/ijmse.4525]

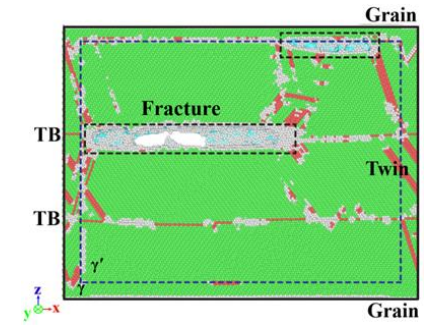

(g)

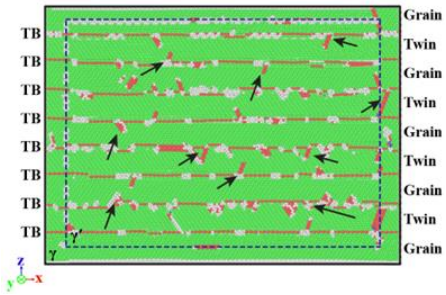

(h)

(i)

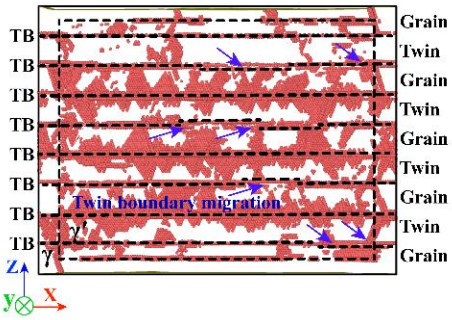

(j)

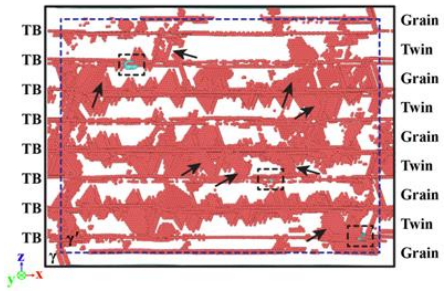

(k)

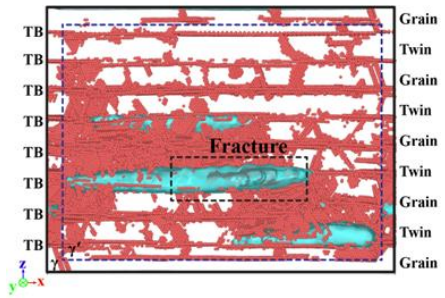

(l)

Fig. 6. (a) Two-dimensional atomic configurations and cross-sectional views of the TB2 model showing the evolution of dislocations and deformation at $\varepsilon = 0.031$; (b) $\varepsilon = 0.0429$; (c) $\varepsilon = 0.04712$; (d) $\varepsilon = 0.05961$; (e) $\varepsilon = 0.06931$, where different slip planes are shown in different colors for clarity; (f) $\varepsilon = 0.07558$; (g) $\varepsilon = 0.112$; (h) two-dimensional atomic configurations and cross-sectional views of the TB8 model illustrating the evolution of dislocations and deformation at $\varepsilon = 0.032$; (i) $\varepsilon = 0.0433$; (j) $\varepsilon = 0.0496$; (k) $\varepsilon = 0.0678$; and (l) $\varepsilon = 0.0891$.

4. Conclusions

Molecular dynamics simulations were performed to investigate the effect of twin-boundary density on the tensile deformation and fracture behavior of a dual-phase γ/γ′ nickel-based superalloy. The results demonstrated that the mechanical role of twin boundaries depended strongly on their number and spacing and could not be described solely in terms of conventional barrier strengthening. In TB1, the isolated twin boundary primarily impeded dislocation motion and increased both the yield stress and yield strain relative to the single-crystal model. By contrast, increasing the number of twin boundaries to two and eight introduced additional twin-boundary planes and twin-boundary/γ–γ′ interface intersections, which acted as preferential sites for earlier dislocation nucleation and consequently reduced the yield stress and strain. Despite this earlier yielding, the post-yield responses of TB2

[DOI: 10.22068/ijmse.4525]

and TB8 were markedly different. In TB2, the two comparatively stable twin boundaries partitioned the model into distinct deformation regions and promoted distributed precipitate shearing, dislocation storage, and sustained strain hardening. As a result, TB2 exhibited the highest ultimate stress among all investigated models and the highest ultimate strain among the twinned models. In TB8, the reduced twin spacing shortened the dislocation mean free path and increased the frequency of dislocation–twin-boundary interactions. This behavior promoted twin-boundary migration, defect rearrangement, localized strain accommodation, and earlier damage development. Constructed surface-mesh analysis further showed that crack initiation was delayed in TB2 relative to TB1 and TB8. Although TB2 subsequently developed the largest final surface-mesh area, this reflected a more extensive post-initiation damage process rather than earlier cracking. In all twinned models, cracks initiated and propagated predominantly along the twin boundaries and γ/γ′ phase interfaces. Overall, the results reveal a non-monotonic, density-dependent transition from barrier-controlled strengthening in TB1 to deformation-partitioning-assisted hardening in TB2 and boundary-migration-assisted, localization-dominated softening in TB8. This transition provides the principal mechanistic contribution of the present study.

Declaration of generative AI and AI-assisted technologies

During the preparation of this manuscript, the authors used generative AI tools to improve the language, clarity, and readability of the text. After using these tools, the authors carefully reviewed and edited the content as needed and take full responsibility for the accuracy, originality, and integrity of the published work.

References

[1] Dong H, Xu T, Ning T, Liu M, Wu D, Ma H, et al. Atomic simulations on the deformation mechanisms in nano-crystalline Ni-Al series Ni-based superalloy based on grain size, strain rate and temperature. Journal of Materials Research and Technology. 2023.

[2] Xia Z, Gao B, Yu J, Wu S, Essa F. Molecular dynamics study of nano-cutting mechanical properties and microstructural evolution behavior of Ni/Ni3Al phase structure. Journal of Materials Research and Technology. 2022;19:2447-57.

[3] Gao Q, Chen X, Yang P, Xue H, Ding Y, Lu X. Effects of Twin Boundary on Tensile Properties and Deformation Mechanism of Ni–Co Alloy Nanopillars. physica status solidi (b). 2022;259:2100458.

[4] Brandon D. The structure of high-angle grain boundaries. Acta Metallurgica. 1966;14:1479-84.

[5] Liu T, Xia S, Li H, Zhou B, Bai Q. The highly twinned grain boundary network formation during grain boundary engineering. Materials Letters. 2014;133:97-100.

[6] Zhao X, Lu C, Tieu AK, Zhan L, Huang M, Su L, et al. Deformation twinning and dislocation processes in nanotwinned copper by molecular dynamics simulations. Computational Materials Science. 2018;142:59-71.

[7] Zhang Y-Q, Quan G-Z, Zhao J, Yu Y-Z, Xiong W. A review on controlling grain boundary character distribution during twinning-related grain boundary engineering of face-centered cubic materials. Materials. 2023;16:4562.

[8] Tian Y, Ren F, Chen F. Twin-boundary-spacing-dependent strength in gradient nano-grained copper. Materials Today Communications. 2022;33:104836.

[9] ZHANG Y-q, JIANG S-y. Molecular dynamics simulation on mechanisms of plastic anisotropy in nanotwinned polycrystalline copper with {111} texture during tensile deformation. Transactions of Nonferrous Metals Society of China. 2021;31:1381-96.

[10] Song H-y, Li Y-l. Effect of twin boundary spacing on deformation behavior of nanotwinned magnesium. Physics Letters A. 2012;376:529-33.

[11] Stukowski A, Albe K, Farkas D. Nanotwinned fcc metals: Strengthening versus softening mechanisms. Physical Review B—Condensed Matter and Materials Physics. 2010;82:224103.

[12] Zhang L, Xin H, Zhao D, Li Z, Ma S. Effect of twin boundary density on mechanical behavior of Al0. 1CoCrFeNi high-entropy alloy by molecular dynamics simulation. Frontiers in Materials. 2022;9:849051.

[13] Tran A-S. Influences of grain size and twin boundary on the tensile properties of nanocrystalline face-centered cubic Cu50Ni50 alloy. Molecular Simulation. 2022;48:1256-68.

[14] Wang Y-J, Tsuchiya K, Dai L. Size-dependent plastic deformation and failure mechanisms of nanotwinned Ni3Al: insights from an atomistic cracking model. Materials Science and Engineering: A. 2016;649:449-60.

[15] Zhang Z, Yang Z, Lu S, Harte A, Morana R, Preuss M. Strain localisation and failure at twin-boundary complexions in nickel-based superalloys. Nature communications. 2020;11:1-11.

[DOI: 10.22068/ijmse.4525]

[16] Shi H, Chen K, Shen Z, Wu J, Dong X, Zhang L, et al. Twin boundary characters established during dynamic recrystallization in a nickel alloy. Materials Characterization. 2015;110:52-9.
[17] Li Y-L, Wu W-P, Ruan Z-G. Molecular dynamics simulation of the evolution of interfacial dislocation network and stress distribution of a Ni-based single-crystal superalloy. Acta Metallurgica Sinica (English Letters). 2016;29:689-96.
[18] Hirel P. Atomsk: A tool for manipulating and converting atomic data files. Computer Physics Communications. 2015;197:212-9.
[19] Chen B, Wu W-P, Chen M-X, Guo Y-F. Molecular dynamics study of fatigue mechanical properties and microstructural evolution of Ni-based single crystal superalloys under cyclic loading. Computational Materials Science. 2020;185:109954.
[20] Plimpton S. Fast parallel algorithms for short-range molecular dynamics. Journal of computational physics. 1995;117:1-19.
[21] Liu H, Wang X, Liang H, Zhao Z, Li L, Yue Z, et al. The effect of void defect on the evolution mechanisms of dislocations and mechanical properties in nickel-based superalloys by molecular dynamics simulation of real γ/γ′ structures. International Journal of Solids and Structures. 2020;191:464-72.
[22] Khoei A, Eshlaghi GT, Shahoveisi S. Atomistic simulation of creep deformation mechanisms in nickel-based single crystal superalloys. Materials Science and Engineering: A. 2021;809:140977.
[23] Ren J, Gui Y, Gao Q, Wang Q, Bai Y, Li J, et al. Mechanical response and plastic deformation in single-and dual-phase polycrystalline FeNiAl alloys: molecular dynamics analysis. Journal of Materials Science. 2024:1-15.
[24] Heydari H, Nourbakhsh SH, Zolfaghari M. Impact of the twin boundary on nickel-based superalloy behavior during tensile deformation using molecular dynamics. Journal of Materials Science. 2025;60:5211-31.
[25] Nosé S. A unified formulation of the constant temperature molecular dynamics methods. The Journal of chemical physics. 1984;81:511-9.
[26] Stukowski A. Visualization and analysis of atomistic simulation data with OVITO–the Open Visualization Tool. Modelling and Simulation in Materials Science and Engineering. 2009;18:015012.
[27] Stukowski A, Albe K. Extracting dislocations and non-dislocation crystal defects from atomistic simulation data. Modelling and Simulation in Materials Science and Engineering. 2010;18:085001.
[28] Fu R, Rui Z, Dong Y, Luo D, Yan C. Effects of γ/γ lamellar interfaces on interlamellar crack propagation behaviors of TiAl alloys. Computational Materials Science. 2021;194:110428.
[29] Duan F, Li Q, Shen Z, Jiang Z, Liu W, Yan Y, et al. Anisotropic mechanical properties and deformation mechanisms of nanotwinned Ni and Ni alloys with extremely fine twin boundary spacings. Acta Materialia. 2023;260:119311.
[30] Shabib I, Miller R. A molecular dynamics study of twin width, grain size and temperature effects on the toughness of 2D-columnar nanotwinned copper. Modelling and Simulation in Materials Science and Engineering. 2009;17:055009.
[31] Lasalmonie A, Strudel J. Interfacial dislocation networks around γ′ precipitates in nickel-base alloys. Philosophical Magazine. 1975;32:937-49.
[32] Yu J, Dong C, Zhang Q, Li B, Liu R. Temperature and crystal orientation dependence of dislocation slip and twin nucleation in bilayer Ni/Ni3Al interface. Computational Materials Science. 2019;162:162-70.
[33] Wang X, Liu J, Jin T, Sun X. Tensile behaviors and deformation mechanisms of a nickel-base single crystal superalloy at different temperatures. Materials Science and Engineering: A. 2014;598:154-61.
[34] Stukowski A, Albe K, Farkas D. Nanotwinned fcc metals: Strengthening versus softening mechanisms. Physical Review B. 2010;82:224103.
[35] Li L, Zhang Z, Zhang P, Wang Z, Zhang Z. Controllable fatigue cracking mechanisms of copper bicrystals with a coherent twin boundary. Nature communications. 2014;5:3536.
[36] Wang H, Rimoli JJ, Cao P. Dislocation mechanisms in strengthening and softening of nanotwinned materials. Journal of Applied Physics. 2023;133.

[DOI: 10.22068/ijmse.4525]